Fatigue crack growth in mooring chain steel at different mean load levels

Vidar Hellum [a,*], Øystein Gabrielsen [b], Sigmund Kyrre Ås [c]

[a] University of Agder, NO-4879, Grimstad, Norway
[b] Equinor ASA, Trondheim, Norway
[c] Department of Marine Technology, NTNU, NO-7491, Trondheim, Norway

ABSTRACT

The fatigue crack growth rates of R4 mooring chain steel at different R-ratios are investigated. Crack growth experiments are performed at three different R-ratios, 0.1, 0.3 and 0.7, utilizing compact tension specimens in air environment. Huang and Moan's driving force parameter ΔK_E, which relates the growth rates at different R-ratios to those obtained at $R = 0$, is explored and adapted for R4 steel.

A full-scale fatigue experiment involving a chain assembly with an identified crack is presented, where the observed crack growth was successfully modelled by the proposed crack growth model.

Case studies with different mean loads are explored where the crack growth model is utilized to predict the fatigue life of $D = 145$ mm chain links with a crack at the crown location. The crack growth simulations are compared and discussed against published S–N curves for chain links with varying mean load. The S–N curves may give very inaccurate results when extrapolated outside of the underlying test data. The crack growth model predicts longer lives at low stress ranges and low mean loads compared to the S–N curves, indicating that current guidelines may be overly conservative in these conditions.

1. Introduction

1.1. Recent research on tension-tension fatigue in mooring chains

Following a comprehensive survey of offshore mooring chain failures, it was reported that 44% of the failures were related to fatigue [1]. This survey included 61 failures, which highlights the need for a better understanding of the fatigue mechanism in mooring chain steel. Recently, several research projects have been initiated to investigate the tension-tension fatigue performance of mooring chains, where some of the main findings can be summarized.

- Residual stresses imposed by manufacturing and proof loading lead to large compressive stresses at the fatigue hot spots [2,3].
- Changes to the residual stresses following cyclic loading [2,4].

Nomenclature

|	
a	crack depth
a_0	initial crack depth
c	half the crack width
C	intercept parameter in Paris equation
C_0	intercept parameter in Paris equation for $R = 0$ curve
D	diameter of chain link
E_i	residual for datapoint i used during linear regression analysis
K	stress intensity factor
K_{op}	stress intensity factor for crack opening load
m	slope of SN-curve/crack growth rate exponent in Paris equation
M	correction factor in Huang and Moan's model
n	number of datapoints
N	stress cycle
R	stress ratio
Y	geometrical correction factor
Y_B	geometrical correction factor for bending stresses
Y_M	geometrical correction factor for membrane stresses
β	parameter in Huang and Moan's model
β_1	parameter in Huang and Moan's model
ΔT	tension range in mooring line
ΔK	stress intensity factor range
ΔK_E	Huang and Moan's crack growth driving force parameter
ΔK_{eff}	effective stress intensity factor range
ΔK_{min}	minimum stress intensity factor within the load cycle
ΔK_{max}	maximum stress intensity factor within the load cycle
ΔK_{th0}	threshold value for the stress intensity factor range at $R = 0$
$\Delta \sigma_B$	bending stress range
$\Delta \sigma_M$	membrane stress range
σ	stress
σ_{max}	maximum stress during a load cycle
σ_{min}	minimum stress during a load cycle
σ_{res}	residual stress

Abbreviations

BSI	The British Standards Institution
DNV	Det Norske Veritas
FEA	finite element analysis
IIW	International Institute of Welding
LEFM	linear elastic fracture mechanics
MBL	minimum breaking load
ML	mean load

- Fatigue performance in full-scale tests of new and used mooring chains is highly influenced by the mean load and the surface condition of the links [5–13].

The full-scale fatigue testing programs also gave an indication of how frequent fatigue fractures occurred at the different fatigue hot spots on the chain link. The fatigue hot spots are shown in Fig. 1 whereas the reported failure locations from different works are shown in Table 1.

Based on the full scale fatigue tests and subsequent statistical works the recommended practice for fatigue design of chain links provided by DNV is now about to be adjusted to include parameters accounting for mean load and surface condition [14]. However, there is still a lack of knowledge regarding the physical process of fatigue crack growth in mooring chains. This is a concern if empirical fatigue life prediction models are extrapolated outside what is covered by the underlying tests, for example at higher or lower mean loads, or higher and lower tension ranges than what has been tested.

In the present work we are seeking better understanding of the crack growth phase at different mean load levels. The mean load effect is particularly important for mooring chains since the mooring line is tensioned to a chosen pre-tension level which highly influences the mean load.
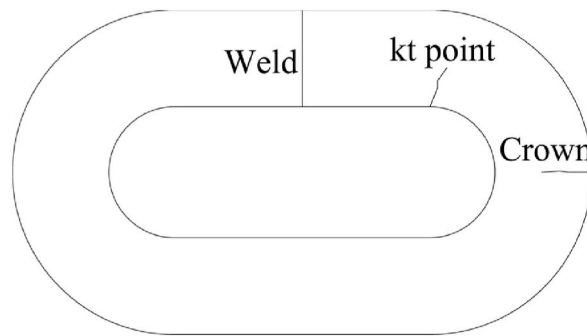
Fig. 1. Mooring chain link with indication of weld, fatigue hot spot at inner bend, often called the kt-point (4 places) and fatigue hot spot at crown (2 places).

Table 1
Number of reported failures at the different locations from full-scale tests of mooring chains by different authors.

	Crown	Inner bend (kt point)	Straight
Fernandez et al. (new chains) [13]	6	9	3
Gabrielsen et al. (used chains) [5]	39	6	1
Zhang and Smedley (new chains) [7]	45	17	15

1.2. The fatigue process in mooring chains

The fatigue process is separated into different stages: Crack nucleation, short crack growth, and long crack growth. It is common to denote the nucleation and short crack growth stages as "initiation", i.e. the initiation of a long crack. In air or inert environments, each of these stages are associated with threshold conditions that must be satisfied in order for cracks to traverse from one stage to the next [15]. The thresholds are associated with microstructural barriers that are removed or significantly reduced in corrosive environments [16]. The nucleation stage can be disregarded in engineering structures since surface roughness and microstructural defects will instantly initiate short cracks [16]. The growth rate of short cracks is highly microstructure dependent, characterized by deceleration and deflection at grain boundaries, and a plastic zone size that is large compared to the crack length. Distinguishing the transition crack length from short to long cracks thus depends on the material properties, ranging from ≤10 μm in high strength steels to 0.1–1 mm in low strength materials [17]. For long cracks, the crack tip plastic zone is small compared to the crack length, and linear elastic fracture mechanics (LEFM) models are commonly adopted for predicting the growth rate using the stress intensity factor range ΔK as the driving force.

Full-scale fatigue tests of new mooring chains at mean load of 20% MBL shows that the S–N curve slope m is close to 3 [13,18] in both air and seawater environments. This indicates that the nucleation/short crack growth phase in mooring chains is negligible compared to long crack growth at this mean load level [19]. This is due to surface defects such as notches and non-metallic inclusions that are much larger than the short/long crack transition length, which means that the size of defects or notch depths may be used as an initial crack length in LEFM analyses [20]. An approach based on Paris' law and an initial flaw size is therefore expected to give good results for mooring chains. This is also supported by the findings in a recent study by Qvale et al. [21] on crack initiation in R4 mooring chain steel.

The Paris crack growth model can be calibrated to include short crack growth with the use of an equivalent initial flaw size, as recommended by e.g. IIW [22] and BSI [23]. The LEFM model may also be combined with fatigue nucleation/initiation models in a two-stage approach, as described in Refs. [24–26].

In the present work, long crack growth is assumed to dominate the fatigue life, and experiments are performed to investigate the crack growth rates of R4-mooring chain steel in air at different R-ratios. Crack growth experiments for mooring chain steel have been performed earlier, e.g. in Refs. [27,28], however, the difference in growth rate at different R-ratios needs further investigation. The aim of the present work is to modify the crack growth driving force parameter based on R-ratio. This will be done by correlating the driving force parameters to R4 crack growth tests performed at different R-ratios in air environment. Furthermore, the model is extended to incorporate growth rates in sea water by investigating existing crack growth test results of mooring chain steel in sea water.

1.3. Crack growth equation for LEFM

A well-established method for estimating the crack growth rate in Linear Elastic Fracture Mechanics is the power law proposed by Paris et al. [29];

$$\frac{da}{dN} = C\Delta K^m \tag{1}$$

Where C and m are material parameters.

In Eq. (1), the stress intensity factor range ΔK is the driving force. The stress intensity factor range is given by:

$$\Delta K = K_{max} - K_{min} \tag{2}$$

Where K is defined as

$$K = Y\sigma\sqrt{\pi a} \tag{3}$$

where Y is a geometry factor and a is the crack depth. The Paris equation is normally conceived to describe the log-linear relationship between ΔK and da/dN in what is denoted the Paris region of the crack growth curve. Hence the parameters C and m in Eq. (1) are determined by simple linear regression by minimizing the square sum of the residuals E_i for the crack growth measurements in the Paris region. An idealized crack growth curve can be seen in Fig. 2 along with typical crack growth measurements determined from experiments.

1.4. Crack closure and driving force models for modelling the R-ratio effect

Many researches have proposed improvements to Paris' law as elaborated by Chowdhury and Sehitoglu [30]. These improvements were deemed necessary based on observations where Paris' law would struggle to predict the growth rate of test specimens under certain conditions. One of the first major improvements was the discovery of the crack closure effect, which was first introduced by Elber [31]. Elber noticed that the crack would partially close during unloading before reaching K_{min}, caused by accumulation of plastically deformed material on the crack faces in the wake of the crack tip. This plasticity induced crack closure occurred even when the whole stress range was in tension. The assumption made by Elber was that the crack growth would only proceed when the crack faces were completely separated, thus the part of ΔK corresponding to when the crack faces were in contact would not contribute to crack growth. The effective stress intensity factor range was defined as:

$$\Delta K_{eff} = K_{max} - K_{op} \tag{4}$$

In Eq. (4), K_{max} is the stress intensity factor at maximum load and K_{op} is the stress intensity factor for the crack opening load. This implies a dependence on the R-ratio since at higher R-ratios, the crack will be open at a larger portion of ΔK.

Several authors soon argued that it was difficult to correlate crack closure measurements with measured crack growth rates. Crack closure has been shown to depend on not only R, but also constraint, material properties, load variations and environment [32]. Hertzberg et al. [33] performed experiments where shims were inserted in the crack mouth to simulate crack closure. Their experiments indicated that parts of the load range below the opening load would also contribute to crack growth.

Vasudevan and Sadananda [34] argue that another effect of the plasticity at the crack tip namely the formation of, or change in local residual stresses at the crack tip region alter the growth rate when the R-ratio changes. Hence, they argue that the local in situ stress state at the crack tip region dependent on the loading history must be included when predicting the crack growth rate. This also means that the compressive part of the stress range may play an important role as further shown by for example Silva [35]. Due to the different mechanisms involved, it is argued that for engineering purposes, the growth rate da/dN at different R-ratios is better estimated by relating the damaging part of ΔK directly to the R-ratio in what is referred to as driving force models. Consequently, empirically established driving force models for estimating crack growth at different R-ratios have been proposed by several authors [36–41].

One of the more recent models was proposed by Huang and Moan [39] where a new driving force parameter ΔK_E, based on the R-ratio and ΔK was proposed as shown in Eqs. (5)–(7).
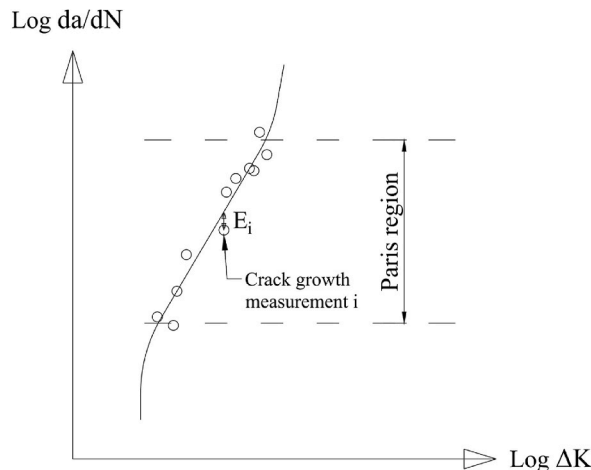

Fig. 2. Sketch showing a fitted crack growth curve to crack growth test measurements.

$$\frac{da}{dN} = C\Delta K_E^m \tag{5}$$

$$\Delta K_E = M\Delta K \tag{6}$$

$$M = \begin{cases} (1-R)^{-\beta_1} & (-5 \le R < 0) \\ (1-R)^{-\beta} & (0 \le R < 0.5) \\ \left(1.05 - 1.4R + 0.6R^2\right)^{-\beta} & (0.5 \le R < 1) \end{cases} \tag{7}$$

By deriving the material constants β and β_1 from test results at different R-levels, Huang and Moan argues that a reasonable description of the test results is obtained by a single curve given by Eq. (5), where C and m values are derived at $R = 0$. The basic assumption is thus that ΔK_E represents a relationship between the damaging part of the stress intensity factor range at different R-ratios. The R-ratio is established by Eq. (8), which ensures that the stress gradient is accounted for.

$$R = \frac{K_{min} + K_{res}}{K_{max} + K_{res}} \tag{8}$$

The model is interesting for mooring chains since it can handle negative R-ratios as well as being flexible to calibration. The β_1 parameter for negative R-ratios is found by Huang and Moan to be an almost constant value close to 0.84 for steel materials [40]. Hence this is adopted in the present paper. However, the β parameter for positive R-ratios should be established by experiments for each separate material which for R4 steel is one of the main goals in the present paper.

1.5. Organization of this paper

This paper is concerned with the mean load effect on the fatigue life of mooring chains and is structured the following way:

In section 1.1 recent research on tension-tension fatigue in mooring chains was presented where it was shown that the mean load and thus the R-ratio is of outmost importance.

Sections 1.2 and 1.3 were concerned with the fatigue process where it was discussed why fracture mechanics may be a suitable fatigue life prediction tool for mooring chains and the basic equations for Linear Elastic Fracture Mechanics was presented.

Section 1.4 was dedicated to discussing the possible mechanisms causing the R-ratio effect and proposed models for incorporating the R-ratio effect. The model by Huang and Moan which will be used in the present work was presented.

Section 2 covers crack growth experiments performed in the present work where crack growth data are plotted for three different R-ratios, regression lines are presented and a parameter for the Huang Moan model is proposed.

Section 3 covers some necessary discussions following the experiments.

In section 3.1 it is argued that the main purpose of the experiments is to investigate the R-ratio effect and we argue that for long crack growth this can be done independently of environment, hence that R-ratio effect obtained in air may be transferred to sea water. The argumentation is based on investigating experimental results from the literature.

In section 3.2 the choice of free corrosion crack growth curve is discussed.

In Section 4 a full-scale experiment where crack growth was monitored on a full-scale link is presented.

Section 5 is dedicated to present the crack growth model for mooring chain steel which incorporates the R-ratio effect.

In Section 6 the crack growth model is utilized to predict the fatigue crack growth of mooring chains and the results are compared to the presented full-scale experiment and recently developed S–N curves from full scale test data found in the literature.

In section 6.1 necessary stress calculations for the crack growth predictions are presented.

Section 6.2 is concerned with discussing the crack growth predictions compared to the full-scale experiment.

In section 6.3 the crack growth predictions are compared to S–N curves where the R-ratios at different combinations of tension ranges and mean load are highlighted.

In section 7 concluding remarks are made.

2. Small-scale crack growth experiments for investigating the R-ratio effect

2.1. General

The purpose of the present experiments is to establish a relationship between the damaging part of the stress intensity factor range at different R-ratios for R4 mooring chain steel. The experiments are performed with compact tension (CT) specimens according to ISO12108 [42] in air environment at three different R-ratios. K increasing tests are performed, where the load range is kept constant during each test.

Table 2
Material properties of R4 steel used for small scale experiments (Material 1).

σ_y [MPa]	σ_u [MPa]
832	927

The yield and ultimate strength of the material is based on available material certificates and is found in Table 2.

Crack mouth opening is measured by an ISO 9513 class 0.5 clip gage and the crack growth is established by the compliance method. Additionally, ink injection has been performed after pre-cracking and the test is stopped before it exceeds the validity range related to remaining ligament given in the ISO standard. After the experiment is stopped, the specimen is broken apart which leaves the crack front at the end of the test clearly visible together with the marked crack front after pre-cracking. These two marked crack fronts are further used to correlate crack depth with measurements. Further descriptions of the test specimens, the test equipment and the measurement equipment are found in Appendix A.

2.2. Test results

2.2.1. Regression lines for the different R-ratios

Following the conclusion of the test series, linear regression was performed to establish crack growth curves for each of the three R-ratios. The regression analyses were performed both by keeping m free and by fixing m to the value provided by BS7910. The interval for the test datapoints utilized for the regression analysis are based on the transition points given in BS7910. Hence, for the in-air tests the lower limit for ΔK was set to 11.5 MPa m$^{0.5}$ for $R < 0.5$ and 6.2 MPa m$^{0.5}$ for $R > 0.5$. Above these levels, the crack growth was assumed to follow Paris' law. Parameters for the curves obtained from linear regression are given in Table 3 along with the two curves given in BS7910 for comparison. The curves based on fixed m values are plotted in Fig. 3 together with the datapoints included in the regression analyses.

The $R = 0.1$ and the $R = 0.3$ curves lie almost exactly on top of the BS7910 $R < 0.5$ curve. Hence, these three curves appears as one solid curve in the graph. This indicates that the closure level is very similar at these R-ratios. The obtained $R = 0.7$ curve lies below the BS7910 $R > 0.5$ curve which indicates a lower crack growth rate at higher R-ratios for the R4 chain steel than for those represented by the BS7910 curve. However, the small number of tests provided here makes it difficult to conclude on this. On the other hand, the $R = 0.7$ curve lies well above the $R < 0.5$ curve provided by BS7910 and the regression lines for $R = 0.1$ and $R = 0.3$.

A few of the experiments were initiated at low ΔK levels to investigate the growth rates near the assumed crack growth threshold. In Fig. 4, where the datapoints near the threshold level is shown, only the $R = 0.1$ results show a clear indication of a steeper curve in the region of the knee point for the BS7910 curve.

2.2.2. Establishing β value and crack growth curve for R = 0

Since all test datapoints are obtained by experiments at positive R-ratios, β can be established from these test series. The same datapoints utilized for the regression analyses for finding the crack growth curves are included in the analysis for finding the optimized β value, and the regression line at $R = 0.1$ with fixed $m = 2.88$ is utilized. When using the procedure described in Appendix B, the following is obtained:

$$\beta = 0.0946$$

And the crack growth curve at $R = 0$ can be represented by:

$$\text{Log } C_0 = -11.0951$$

$$m = 2.88$$

In Fig. 5 the datapoints from the test series are plotted as function of ΔK and ΔK_E respectively.

From this section it can be concluded that the differences in crack growth rate between the different positive R-ratios are small. This is also seen when comparing the regression lines from the different R-ratios in section 2.2.1. In the second paper by Huang et al. [40] where this model is discussed a general expression for calculating β is proposed where the value is close to 0.22 in the Paris region of the curve. The β value of 0.0946 obtained for R4 steel thus indicates smaller differences between positive R-ratios for this material.

3. Calibration of crack-growth model

3.1. Testing in air vs testing in seawater with free corrosion

In the present work the crack growth experiments are performed in air environment. The main outcome from the experiments is the

Table 3
Parameters obtained for the regression lines.

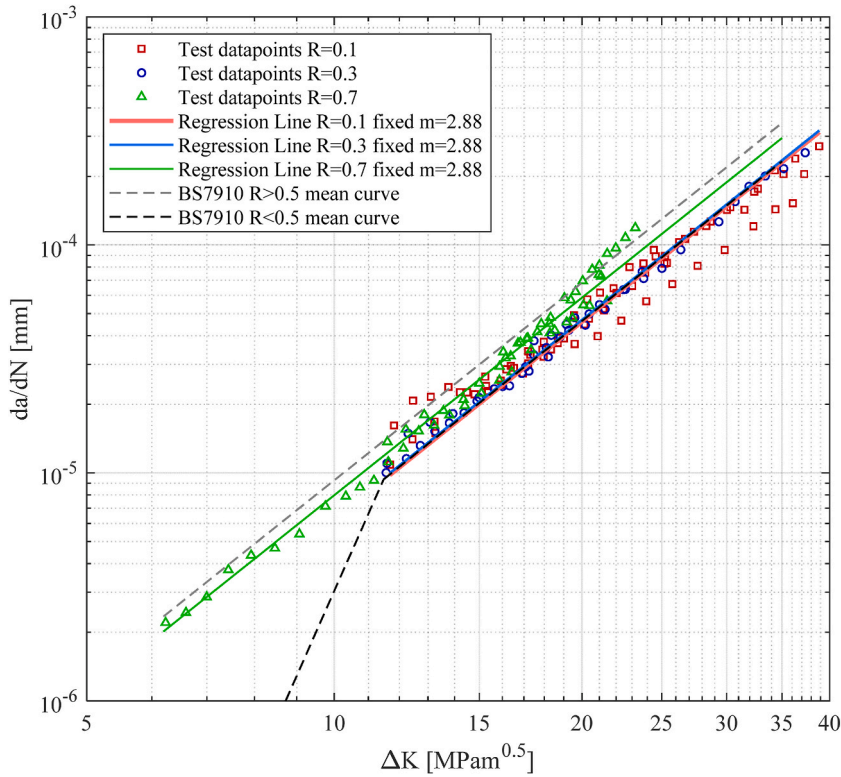|	Regression lines			
	log C	m	Log C (fixed m)	Fixed m
R = 0.1	−10.48	2.43	−11.083	2.88
R = 0.3	−10.864	2.71	−11.076	2.88
R = 0.7	−11.073	2.96	−10.978	2.88
BS7910 R < 0.5			−11.080	2.88
BS7910 R > 0.5			−10.912	2.88

Fig. 3. Test datapoints used for regression analyses plotted along with the regression lines.
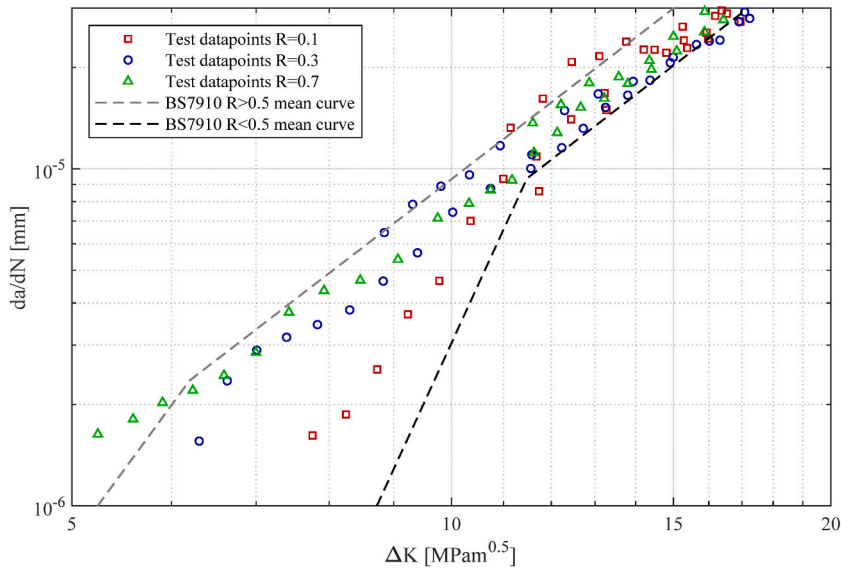

Fig. 4. Test datapoints near the transition points of the BS7910 curves.

β value which is a key parameter to establish ΔK_E. Mooring chains are subject to free corrosion in seawater, thus a key question is how to account for this based on fatigue tests performed in air environment. The hypothesis for our approach is that the corrosion fatigue is only related to the damaging part of ΔK, which is accounted for when using ΔK_E as the driving force parameter. The increased growth rate under corrosion will only occur during the damaging part of ΔK. In other words, during the non-damaging part of ΔK when no crack growth occurs, there is no interaction between corrosion and crack growth. A baseline crack growth curve at a single R-ratio can then be established for free corrosion, and the R-ratio effect may be investigated separately in air. To investigate this hypothesis
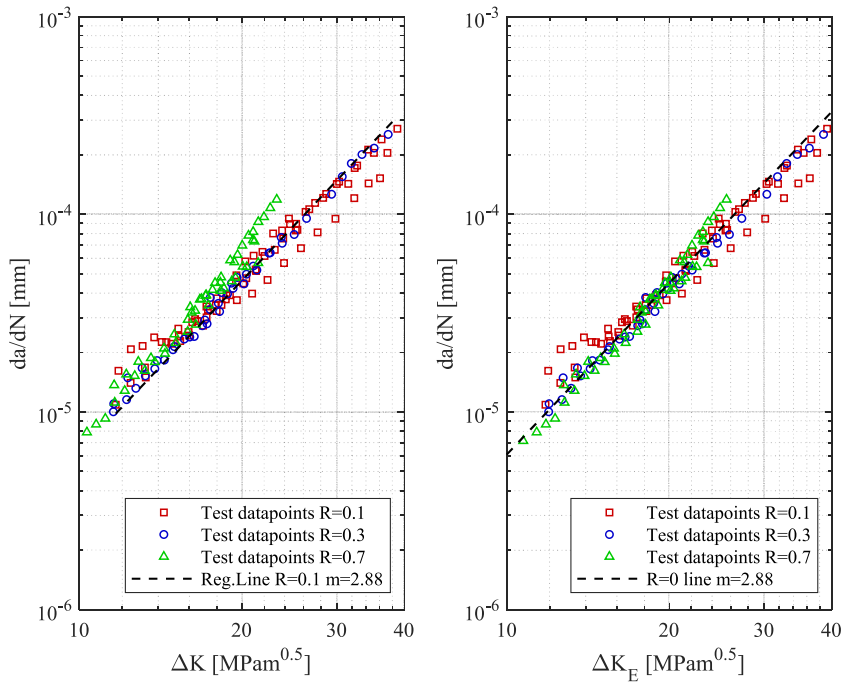
Fig. 5. Test results represented by ΔK (left) and ΔK_E (right).

further, experiments performed by Vosikovsky [43] are explored. An overview of the test series for X70 steel can be seen in Table 4:

The tests cover different *R*-ratios for the same material in both air and free corrosion in artificial seawater. The free corrosion tests were performed at 0.1 Hz, which justifies full effect of corrosion fatigue crack growth. Test results for 10 MPa m$^{0.5}$ < ΔK < 30 MPa m$^{0.5}$ are included in the present analysis.

If the hypothesis that corrosion fatigue crack growth is only related to the damaging part of ΔK is valid, it should be possible to establish a single value of β which is common for the air and free corrosion test series of Vosikovsky. Further, it should be possible to unify the test results around the two curves at $R = 0$ for air and free corrosion respectively using this β value.

To test this the following procedure was followed.

1. Linear regression of the Vosikovsky test results at $R = 0.05$ obtained in air on a log-log scale
2. Find the value of β that minimizes the square sum of the residuals (E_i) when expressing the test data for all *R*-ratios in air as ΔK_E vs da/dN relative to the curve found from linear regression.
3. Use the obtained value of β to construct a curve for $R = 0$ based on the curve obtained at $R = 0.05$ and the procedure described in Appendix B
4. Linear regression of the Vosikovsky test results at $R = 0.05$ obtained in artificial seawater with free corrosion on a log-log scale
5. Use the obtained value of β from tests in air to construct a curve for free corrosion at $R = 0$ based on the C and m values for free corrosion obtained at $R = 0.05$
6. Expressing the datapoints for free corrosion as ΔK_E vs da/dN, where ΔK_E is based on the β value from tests in air
7. Compare the square sum of residuals (E_i) and the standard deviation *s* obtained for air and free corrosion tests respectively when using the value of β obtained from the tests in air

Following this procedure, a β value of 0.2039 was established for the X70 steel based on the test results in air. The representation of the test results via ΔK and ΔK_E for air environment is shown in Fig. 6. Now the same value of β was used for plotting the test results in

Table 4
Crack growth test series performed by Vosikovsky.

Material	Yield strength	Environment	*R*-ratio
X70	527	Air	0.7
X70	527	Air	0.4
X70	527	Air	0.05
X70	527	Free Corrosion	0.7
X70	527	Free Corrosion	0.4
X70	527	Free Corrosion	0.05

artificial saltwater by ΔK_E as shown in Fig. 7.

From Figs. 6 and 7, it is evident that for both environments the R-ratio effect can be modelled with the Huang Moan model utilizing a single β value. The standard deviation given in Table 5 is slightly higher for free corrosion than for air. An additional exercise was performed where the free corrosion test data were used to obtain a β value directly for the free corrosion data set. This was very close to the value obtained in air and gave the same standard deviation as when using the β value obtained by the air tests. This strongly supports the hypothesis that corrosion fatigue crack growth is related to the damaging part of ΔK, and that investigations of R-ratio effect for long cracks may be performed in air environment. The same conclusion was drawn in a recent study by Adedipe et al. [41].

3.2. Crack growth curve for R4 mooring chain steel with free corrosion at R = 0

To be able to use the Huang-Moan model for crack growth calculations in mooring chain steel it is necessary to obtain a crack growth curve for R4 chain steel in seawater at $R = 0$. Such a curve does not yet exist, but there are two possible options based on the available literature.

The first option is to use a curve obtained by Lassen et al. [27], who performed a relatively small number of crack growth experiments on R4S chain steel. The properties of the R4S steel are close to the properties of the R4 steel, and only a very small deviation between these two steels should be expected. Lassen et al. presented a crack growth curve with slope $m = 2.88$ and C = 21.4E-12 for units MPa and m based on their results from testing in seawater. However, during their work the two datapoints corresponding to the lowest crack growth rates were omitted from the linear regression. When performing regression analysis including all their datapoints we obtain a growth curve close to the ones presented in BS7910. This curve is given by Eq. (9).

$$\frac{da}{dN} = 4.43 \bullet 10^{-12} \Delta K^{3.45} \tag{9}$$

This relatively large change of slope when including two extra datapoints highlights that there is very few datapoints in this analysis. The test series was performed at $R = 0.2$, and from Fig. 8 it is seen that the curve lies between the $R > 0.5$ curve and the $R < 0.5$ curve presented in BS7910, but fairly close to the $R < 0.5$ curve. When utilizing the method described in Appendix B and the β value found in section 2.2.2 the following crack growth curve is established for mooring chains at free corrosion for $R = 0$:

$$\frac{da}{dN} = 4.119 \bullet 10^{-12} \Delta K^{3.45} \tag{10}$$

Here the m value obtained from the regression analysis is kept since it is close to the one provided in BS7910. The $R = 0$ curve is also presented in Fig. 8.

The second option is to use the curve for $R < 0.5$ from BS7910. Zhang et al. [44] argues that the curves given in BS7910 may be extended to high strength steel such as R4 and R5 chain material. Since the difference between the curves discussed here is small, the
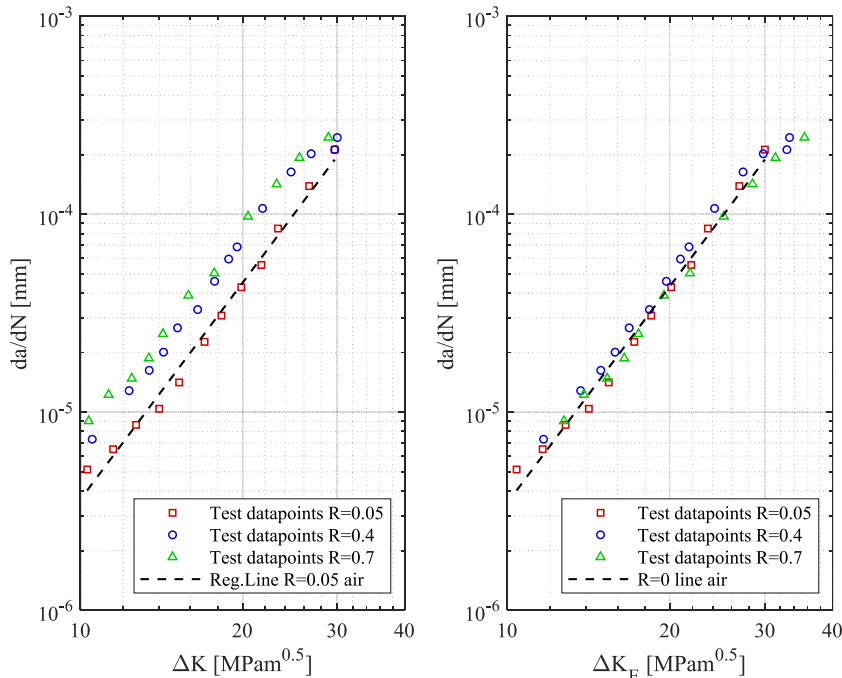

Fig. 6. Test results from Vosikovsky performed in air represented by ΔK (left) and ΔK_E (right).
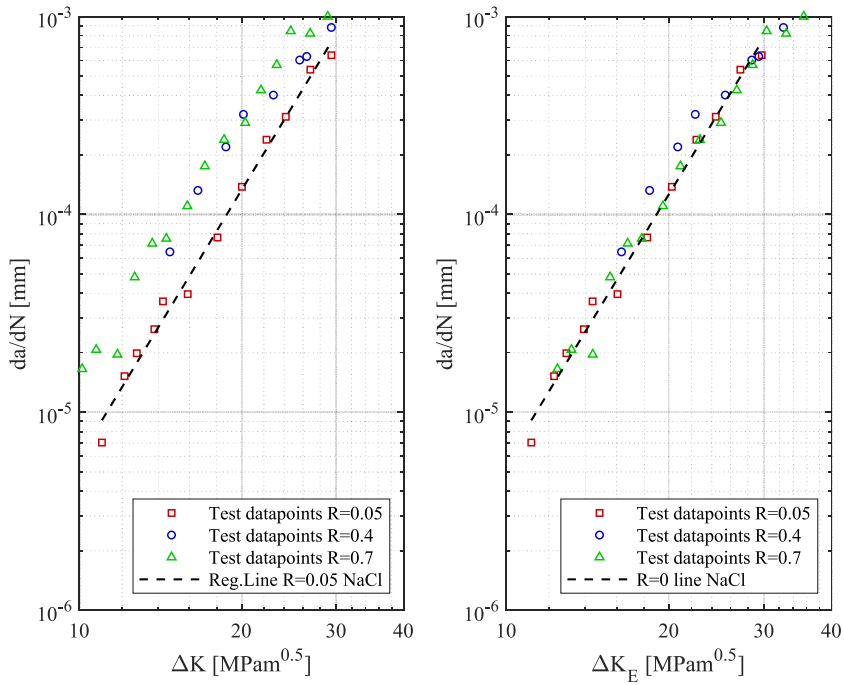
Fig. 7. Test results from Vosikovsky performed in artificial seawater represented by ΔK (left) and ΔK_E (right).

Table 5
Established β, squared sum of residuals and standard deviations for the different environments for X70 steel.

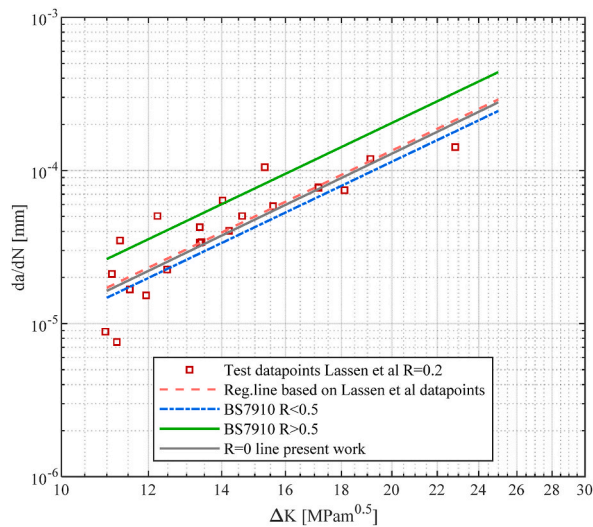|	Air	Free corrosion	
β established from tests in air	0.2039	0.2039	
β established from tests with free corrosion			0.2044
Q^2	0.135	0.29	0.29
s	0.062	0.094	0.094

Fig. 8. Crack growth curves based on Lassen et al. data compared with the curves presented in BS7910.

curve based on Lassen's experiments will be used in the present paper since the *R*-ratio for this test series is known. It should be noted that further research on the baseline crack growth curve in seawater at $R = 0$ should be performed in the future to enhance the credibility of this curve.

4. Full-scale crack growth experiment

In addition to the small-scale experiments for establishing the β value for the Huang-Moan model, a full-scale experiment performed by Equinor, where crack growth was monitored during cyclic loading of a D145mm chain link assembly in artificial seawater has been investigated in the present work. The chain link assembly, consisting of 5 links, was originally part of a mooring line in service in the North Sea before being retrieved. After retrieval the chain link assembly was part of an experiment where only the number of cycles to failure should be recorded. However, the experiment was stopped after 2,091,717 cycles without fracture. During this experiment the chain link assembly was fully submerged in seawater and no crack measurements were performed. When examining the chain link assembly by magnetic particle testing after the experiment was stopped, a 42 mm long crack was detected at the crown of one of the links. Following this, the crack growth experiment was initiated to follow the development of the detected crack.

4.1. Description of the full-scale test

The key parameters for the crack growth experiment are given in Table 6. The same values were also used during the first 2,091,717 cycles, before the crack growth monitoring were initiated. Note that the yield strength of the material used in this full-scale experiment is lower than the yield strength of the material used in the small-scale experiments described earlier. The ultimate strength is on the other hand similar which is the most important for classifying the material as R4. The materials stem from different projects and the material used for the full-scale experiment has a lower carbon content than the material for the small-scale experiments.

A 4 MN test rig was used for the crack growth experiment where the crack location was continuously flooded by artificial seawater by a system consisting of a hose, a pump and a sprinkler. This to avoid using a closed chamber which needed be tapped and dismantled for each crack growth measurement. The test machine is shown in Fig. 9.

4.2. Results

The crack growth was monitored during the experiment by visual inspection (crack length), ultrasonic testing (crack depth) and magnetic particle testing (crack length) at regular intervals. The results from the measurements can be found in Table 7.

The experiment was stopped at a crack depth of 78.3 mm as measured by ultrasonic testing. After dismantling the chain links from the machine, the cracked link was broken apart at the location of the crack and the crack faces were measured. The crack face is shown in Fig. 10. Post-mortem measurement of the crack face revealed that the final crack depth was approximately 52 mm giving a final aspect ratio of $\frac{a}{c} = \frac{52}{65} = 0.8$. This aspect ratio is as expected based on available literature [45,46] which shows that cracks growing in round bars quickly converge towards an aspect ratio close to 0.8. On the other hand, the post-mortem crack depth measurement deviates from the measurement performed by ultrasonic testing. This highlights that the ultrasonic depth measurements are uncertain. With the argument that the crack aspect ratio converges quickly towards $\frac{a}{c} = 0.8$, the crack depth at the start of the crack growth experiment can be estimated to $a = 0.8c = 0.8 \bullet 21mm = 16.8mm$.

With the observed uncertainty regarding the ultrasonic testing the initial crack depth is treated as a value between a $= 16.8$ mm and 21.9 mm when comparing towards simulated crack growth in later sections of the paper. The final crack depth is taken as 52 mm.

5. Crack growth model for mooring chain steel

Crack growth is in the present paper calculated according to Eqs. (11) and (12), which gives the extension in crack depth *a*, and the extension in half the crack length *c* per cycle. The crack growth is calculated incrementally with the increment size given by Eq. (13) where ΔT is the tension range and MBL is the minimum breaking load of the chain. The choice of this increment size has been subject to a sensitivity study shown in Appendix C. Since the crown of the links is the hot spot experiencing most of the fractures during testing, the present paper will focus on the crown for the crack growth simulations.

Table 6
Test parameters.

Chain Diameter [mm]	145
Chain Grade	R4
σ_y [MPa](Material 2)	673
σ_u [MPa] (Material 2)	934
MBL [kN]	18,665
Environment	Artificial seawater (3.5% NaCl)
Tension range [%MBL]	12
Mean Load [%MBL]	9.7
Test frequency [hz]	0.5

Fig. 9. Test machine for full-scale experiment.

Table 7
Measurements during full scale test.

Interval cycles	Cycles CG experiment	Cycles Total	Measured length by Magnetic Particle Testing (2c) [mm]	Measured depth by Ultrasonic Testing (a) [mm] (Post-mortem measurement) {Estimated lower limit of start depth}
0	0	2,091,717	42	{16.8} 21.9
7299	7299	2,099,016	47	25.5
11,476	18,775	2,110,492	49.5	26.2
33,458	52,233	2,143,950	71	34.5
21,620	73,853	2,165,570	92	45.5
10,141	83,994	2,175,711	100	51.5
10,000	93,994	2,185,711	110	57.1
7100	101,094	2,192,811	120	65.7
7801	108,895	2,200,612	128	72.4
2750	111,645	2,203,362	130	(52) 78.3

$$\frac{da}{dN} = 4.119 \bullet 10^{-12} \Delta K_{E,a}^{3.45} \tag{11}$$

$$\frac{dc}{dN} = 4.119 \bullet 10^{-12} \Delta K_{E,c}^{3.45} \tag{12}$$

$$Cycle\ increment = \frac{20}{\left(\Delta T / MBL\right)^2} \tag{13}$$

The driving force parameter is given by Eq. (6) and M is established by the following equations:

$$M = \begin{cases} (1-R)^{-0.84} & (-5 \leq R < 0) \\ (1-R)^{-0.0946} & (0 \leq R < 0.5) \\ \left(1.05 - 1.4R + 0.6R^2\right)^{-0.0946} & (0.5 \leq R < 1) \end{cases} \tag{14}$$

Note here that a value of $\beta_1 = 1$ would mean that the compression part of the stress range does not contribute to crack growth, whereas $\beta_1 < 1$ means that the compressive part of the stress range will also be damaging to some extent. In our case we are using $\beta_1 =$

Fig. 10. Cross section cutout of a 145 mm chain link, showing the final crack size after fatigue testing. The crack face is darker due to oxidation.

0.84.

The stress intensity factor *K* is obtained based on the membrane and bending stress at the crack location as given in Eqs. (15) and (16).

$$K_a = \left(\sigma_M Y_{M,a} + \sigma_B Y_{B,a} \right) \sqrt{\pi a} \qquad (15)$$

$$K_c = \left(\sigma_M Y_{M,c} + \sigma_B Y_{B,c} \right) \sqrt{\pi a} \qquad (16)$$

The geometry functions *Y* are taken from Ref. [47], and is presented in Appendix D.

The stress normal to the crack faces are determined by FEA and is separated into bending and membrane stress. First a non-linear elastic-plastic analysis is performed to simulate the Proof-Loading of the chain links, where the chain is loaded to approximately 70% of the chain MBL and then unloaded. This introduces high compressive residual stresses at the fatigue hot spots. After unloading during the FE analysis, the residual stresses can be recorded and linearized such that they can be represented as membrane and bending stresses and further used to establish K_{res}.

To establish the stresses from cyclic loading, which is significantly lower in magnitude compared to the proof load, a linear FE analysis is performed. Stress concentration factors are established for bending and membrane stresses respectively as a function of the nominal stress in the link. The *SCF* can then be used to determine the bending and membrane stress at the crown based on the tension *T* applied to the link as given in equations (17) and (18). This is further used to establish K_{min} and K_{max}.

$$\sigma_B = \frac{2SCF_B T}{\pi D^2} \qquad (17)$$

$$\sigma_M = \frac{2SCF_M T}{\pi D^2} \qquad (18)$$

The FE analyses are described in more detail in Appendix E.

When the residual stresses and the operational stresses are established, K_{min}, K_{max} and K_{res} can be determined by equations (16) and (17) which is further used to establish ΔK, R and ΔK_E for the crack growth simulation. Note that only K_a will be used to determine the *R*-ratio in the present paper.

6 Crack growth simulations of D145mm mooring chain steel and comparison with full-scale test and S–N curves

In this section, crack growth modelling will be performed of D145mm chain links of R4 quality. The performance of the crack growth model is discussed based on its ability to simulate the crack development from the full-scale test described in section 4. The crack growth model is then utilized with different mean load levels and tension ranges, and compared and discussed with respect to the S–N curves.

5.1. Stress calculations

FE analyses have been performed as described in section 5.

5.1.1. Residual stresses

The residual stresses were established by simulating the proof loading of the links. The proof load was set to 13079 kN in accordance with DNV [48]. The obtained residual stress distribution over the cross-section height can be seen in Fig. 11 along with the linearization performed which makes it is possible to separate into bending and membrane stresses. The residual stresses are slightly different between the materials used in the small-scale experiments (Material 1) and the full-scale experiment (Material 2)
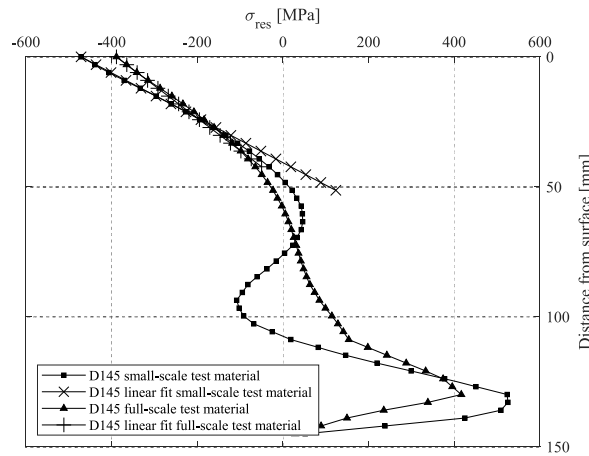
Fig. 11. Residual stress distribution in 145 mm chain link after proof loading.

respectively. The residual stress at the surface is approximately 388 MPa in compression for Material 2 whereas it is 470 MPa in compression for Material 1. Further, the residual stresses are compressive to a depth of around 48 mm for Material 1 and to around 60 mm for Material 2. It should be noted that heat treatments also influence residual stresses in the chain links. However, the heat treatments are performed before proof loading and as argued by Zarandi and Skallerud [2] the residual stresses normal to the most common crack plane during fatigue crack growth will be dominated by the stresses generated from the proof load. As such only the residual stresses from the proof load are included here.

A linearization was performed as also shown in the graph. When separating this linearized stress into bending and membrane stresses the values given in Table 8 are obtained which is used for the crack growth simulations.

5.1.2. Stresses from operational loads

From the linear FE analysis of the links, SCFs for bending and membrane loading was established. Table 9 shows the obtained SCFs. These are included in equations (18) and (19) to calculate the stresses for crack growth simulations.

5.2. Crack growth simulation for comparison with full-scale test

Crack growth has been simulated for comparison with the full-scale experiment described in section 4. The simulation has been performed with Mean Load $ML = 9.7\%MBL$, Tension range $\Delta T = 12\%MBL$ and a final crack size of $a_{final} = 52$ mm. Due to the uncertainty related to the initial crack size, a back calculation has been performed from 52 mm depth to see which initial crack depth would give the recorded 111,645 cycles from the simulation. In this case the final crack aspect ratio $\frac{a}{c} = 0.8$ has been used and the initial aspect ratio has been varied between 0.75 and 0.85. The simulated crack growth is shown in Fig. 12, where it is seen that an initial crack depth of $a_0 = 19.7$ mm gives the recorded number of cycles to reach approximately 52 mm. This initial crack depth is slightly smaller than what was measured by ultrasonic testing in the full-scale experiment. The variation in estimated initial crack depth based on the different initial crack aspect ratios were ∓ 0.1 mm.

In Fig. 13 the development of the R-ratio during the crack growth simulation is shown. The R-ratio starts below -3 and increases to a value between -1 and 0 when approaching 52 mm crack depth and thus remains negative for the whole simulation.

The conclusion from this section is that the crack growth model, which includes the residual stress gradient, can model the crack development recorded from the full-scale experiment. Although the measurement of the initial crack depth from the experiment is uncertain, the crack growth model predicts an initial crack size within the expected range.

Table 8
Residual stresses separated into bending and membrane components.

	$\sigma_{B,res}$ [mPa]	$\sigma_{M,res}$ [mPa]
Material 1	−839	368
Material 2	−581	192

Table 9
SCF for bending and membrane stress at the crown of 145 mm chain links.

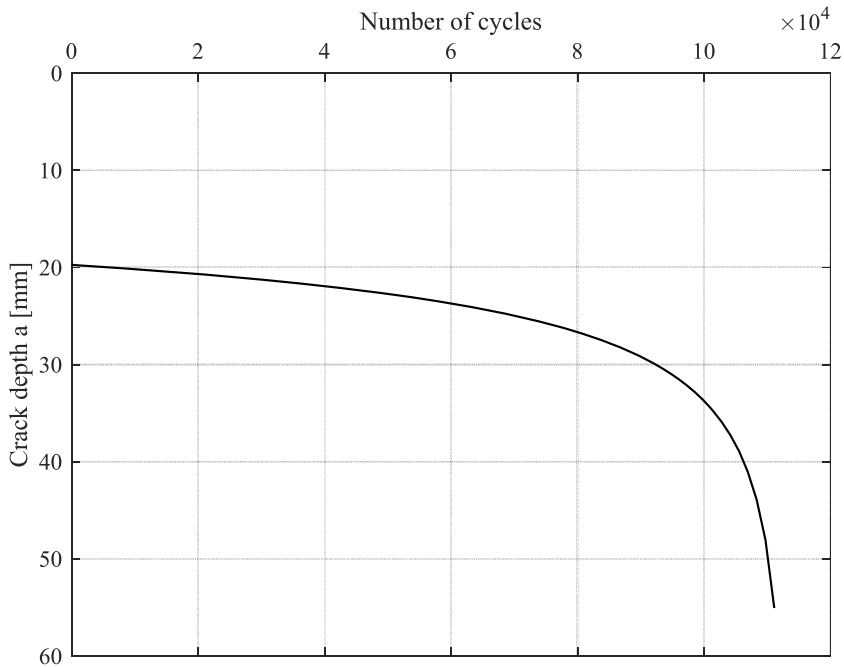| SCF_B	SCF_M
3.458	0.834

Fig. 12. Crack growth simulation for comparison towards full scale test.

5.3. Crack growth simulations for comparison with S–N curves

The crack growth model will be explored next, and compared against recently developed S–N curves that incorporates the mean load as part of the S–N formulation. The curves were published by Lone et al. [11] and also includes surface condition as a parameter. Similar curves were developed from full-scale fatigue tests performed by Fernandez et al. on new chains [49]. The curves from Lone et al. and Fernandez et al. are similar for chains with "as-new" surface condition. The reason for selecting the Lone curves for the present work is the large size of the dataset that was used for obtaining these curves.

Most of the tests are performed with high mean load and with large tension range. When decreasing the mean load, the tension range is normally kept very high to limit the time spent for the tests. Also, there are almost no test performed with mean load above 20%MBL. Hence, there is a lack of knowledge regarding the validity of the proposed S–N curves outside of what has been tested. The
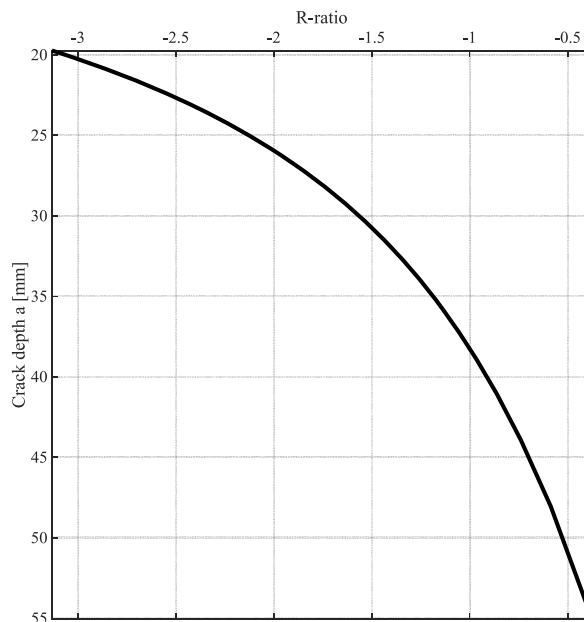

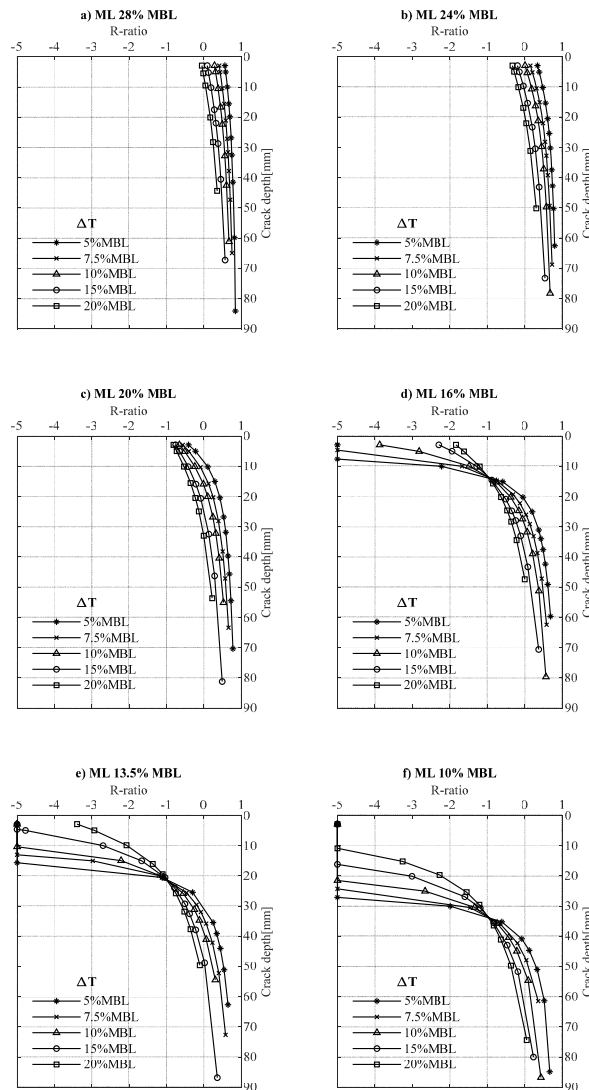**Fig. 13.** R-ratio development from crack depth of 19.7 mm to approximately 52 mm.

Fig. 14. *R*-ratios for the different combinations of Mean Load and Tension ranges.

goal here is therefore to investigate any discrepancies between the S–N curves and the crack growth model predictions.

The crack growth is simulated from a selected start depth of 0.02*D*, which for the 145 mm chain gives a start depth of 2.9 mm, to a final crack size set to *D*/2. This is a rather large start depth, however, measurements of residual stresses performed by Zarandi and Skallerud [2] showed that stresses found from measurements corresponded very well with the stresses found from FEA at this depth. Surface roughness and very small corrosion pits, which could be found on as-new chains, may be of great importance for early crack growth but are believed to have less influence at this depth. Hence, at this depth we have more confidence in the parameters used in the model. The initial aspect ratio is set to $\frac{a}{c} = 0.8$ to limit the scope of the current study.

Simulations have been performed at Mean Loads of 10%MBL to 28%MBL where for each of the mean loads, simulations have been performed with tension ranges from 5%MBL to 20%MBL. The residual stresses are based on the simulations utilizing Material 1 parameters.

The first very interesting result is the *R*-ratios for the different combinations of mean load and tension ranges which are displayed in Fig. 14. For mean loads of 24%MBL and 28%MBL the *R*-ratio is mostly positive except for the first few millimetres of growth at the highest tension ranges. This means that we should expect the crack growth rate to be very similar at these mean loads because of the low value of *β* that was established from the small-scale experiments. But already at a mean load of 20%MBL, the compressive residual stresses lead to negative *R*-ratios for all the tension ranges during the first millimetres of crack growth. If further decreasing the mean load to 16% MBL, the two smallest tension ranges start at the cut-off value of $R = -5$. This means that early crack growth at these tension ranges is as low as it gets with this model, and equal to that obtained when the complete stress range is in compression. For the mean loads of 10%MBL and 13.5%MBL the *R*-ratios further decrease with large parts of the crack growth now at *R* = -5. This means
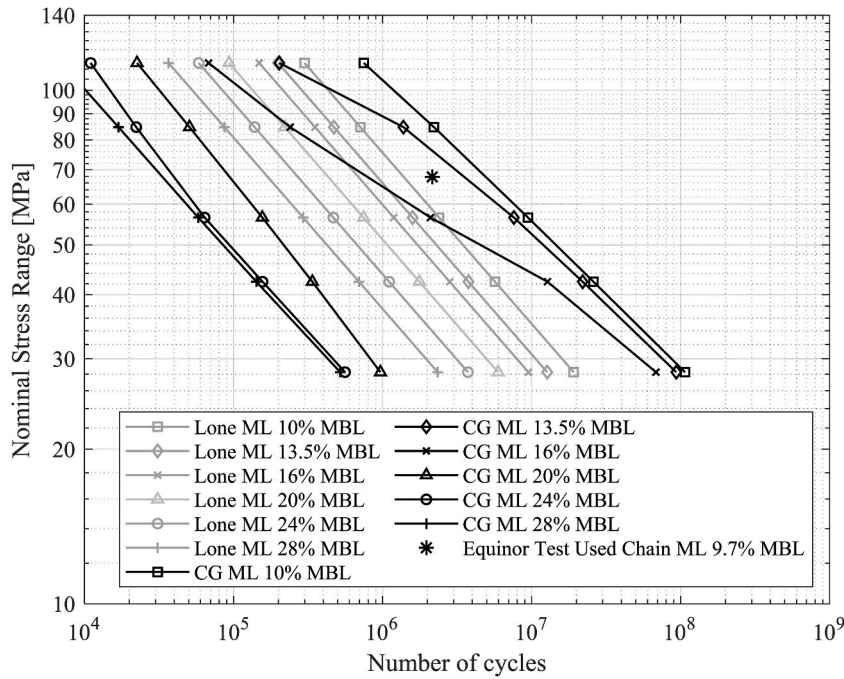
Fig. 15. Crack growth from a crack size of a = 2.9 mm to final crack size of D/2 compared with Lone S–N curves.

that the fatigue crack growth life at the two lowest mean loads should be expected to be similar in the cases where $R = -5$.

The crack growth simulations for the different mean loads and tension ranges are displayed in Fig. 15. For the Mean loads of 20% MBL, 24%MBL and 28%MBL, where positive R-ratios are present, the curves obtained from the crack growth simulations are well below the S–N curves. This is as expected since we are starting from an initial crack of 2.9 mm. Hence, the crack growth before reaching a crack depth of 2.9 mm will cover the larger part of the fatigue life at these mean loads. The slope of these curves are close to 3 which is the slope adopted for the S–N curves. Also as expected, the curves obtained for 24%MBL and 28%MBL are very close to each other since the R-ratio is mainly positive for these mean loads.

However, when studying the crack growth curve for 16%MBL, the slope of this curve is less steep. This is because the R-ratio is rapidly decreasing with decreasing tension range and reaching $R = -5$ for the lowest tension ranges. The crack growth curve from the simulation is still below the S–N curve for the upper part of the curve, but is well above the S–N curve at the lower end.

For the two lowest mean loads, the lower part of the curves are also well above the S–N curves. At the low tension ranges at these low mean loads, the stress range is purely in compression. These tension ranges are more common in service than the higher ranges used during fatigue testing. Hence, fatigue tests of mooring chains at high tension ranges do not capture this beneficial effect that is shown here. It is also interesting to see that the curves for 10%MBL and 13.5%MBL converges at low tension ranges, meaning that further decreasing the mean load below 10%MBL will give little increase in the crack growth part of the fatigue life. Fig. 15 also includes the number of cycles to failure during testing for the link included in the full-scale experiment. However, the cycles spent during its many years in service before being retrieved is not included. This result lies above the S–N curve but below the corresponding crack growth curve.

The trends shown by the crack growth curves when comparing them to the S–N curves are very interesting with respect to the potential for longer lives at lower tension ranges at lower mean loads. The parameters included in the crack growth model have been shown to model the crack growth well compared to the full-scale experiment, which started from a crack size of around 20 mm. When starting the crack growth calculation at 2.9 mm depth, the number of cycles for crack growth are overestimated for the lowest mean loads and highest tension ranges, where testing have been performed. Also, crack growth seems to constitute most of the life for the low mean loads, which indicates that the early crack growth until reaching a crack of 2.9 mm may be less dependent on the mean load compared to the subsequent crack growth. A possible reason for this is relaxation of the residual stresses close to the surface. Also surface roughness and small corrosion pits might accelerate initiation, increase stresses close to the surface, and possibly alter the residual stresses. Hence, there are some uncertainties related to the initiation and early crack growth. It is possible that early crack growth is governed by interactions between different mechanisms, which require a different modelling technique than explored herein.

6. Conclusions

A fracture mechanics model for fatigue crack propagation in mooring chains is presented, including the R-ratio effect due to load level and residual stresses.

Small-scale crack growth experiments were performed at different positive R-ratios. The results from the experiments were used to derive the parameter β for the fracture mechanics model at positive R-ratios. The small value of β that was obtained and the crack

growth curves for the different R-ratios showed that the difference in growth rate between different positive R-ratios are very small.

The obtained experimental results show that at $R = 0.1$, the R4 mooring chain steel show similar growth rates as those predicted by the mean curve recommended by BS7910 for $R < 0.5$. Further, the results indicate that at $R = 0.7$ the R4 mooring chain steel experiences a lower growth rate than what is predicted by the BS7910 $R > 0.5$ curve.

The proposed crack growth model incorporates the gradient of the residual stresses. The combination of stresses from global forces and internal stresses will for many common mooring load scenarios lead to negative R-ratios at the fatigue hot spots. This is a very beneficial effect that might not be fully captured by newly proposed S–N curves that are based on testing at higher stress ranges.

Crack growth simulations at different mean loads show that the combination of low mean load and low stress ranges might impose much less fatigue damage to the chain links than estimated by the S–N curves. This is due to the stress ranges being mostly in compression giving low R-ratios. On the other hand, when reaching the combination of mean load and tension range, which leads to the complete stress range being in compression, further decrease of the mean load will not increase the fatigue crack growth life.

The proposed model showed good ability to simulate the measured crack growth from a full-scale experiment where the crack growth measurements were initiated with a large crack. However, when comparing the simulations towards the S–N curves it also showed that there are uncertainties related to early crack growth.

The findings provided here should encourage further full-scale fatigue testing of mean load and tension range combinations not yet explored. It should also encourage further research on quantifying early stages of crack growth in a chain link.

Analysis of crack growth tests found in the literature at different R-ratios in air and seawater indicate that the effect of R-ratio on long crack growth can be calibrated based on air environment, and subsequently be applied to free corrosion in seawater, if a reference crack growth curve for $R = 0$ is established from testing in seawater. This is promising as fatigue testing in seawater is much more time consuming than testing in air.

Declaration of competing interest

The authors declare that they have no known competing financial interests or personal relationships that could have appeared to influence the work reported in this paper.

Data availability

Data will be made available on request.

Acknowledgments

Appendix A. Test setup

The test procedure is performed according to ISO12108 [42].

Test specimens

The test specimens are cut from chain links which have been in service and are provided by Equinor ref. Figure A.1.

Fig. A.1. Chain links before fabrication of test specimens
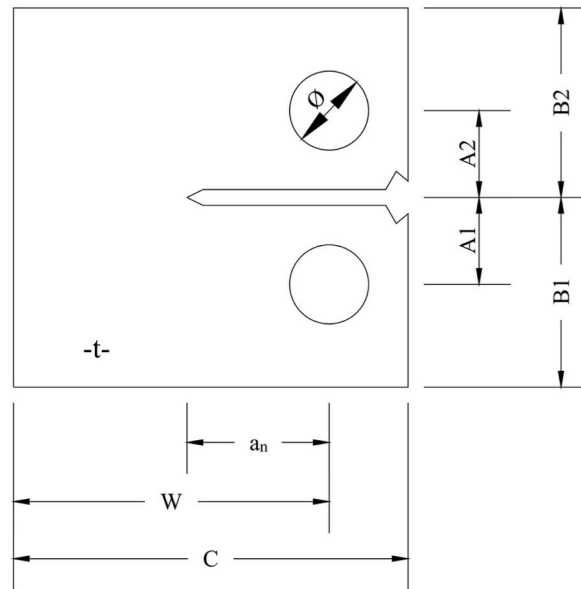
Compact tension (CT) specimens are utilized, as shown in Figure A.2 where the fatigue notch is obtained by electric discharge machining.

Pre-cracking is performed prior to testing in according with the standard and ink injection is performed at the end of pre-cracking to obtain a marked crack front at the start of the test series.

The specimens are marked with the number on the link it has been extracted from, 195 or 196 and the specimen number. An overview of the test specimens used is given in Table A.1.

Table A.1
Test specimen overview

Specimen no.	R-ratio	ΔK_{min} [MPam$^{0.5}$]	ΔK_{max} [MPam$^{0.5}$]
195–1	0.7	16.7	21.5
195–2	0.1	11.1	36.1
195–3	0.3	8.8	21.0
195–6	0.3	6.0	17.1
195–7	0.7	5.2	16.4
195–8	0.7	15.0	23.2
195–9	0.7	16.0	21.0
196–1	0.7	11.6	19.4
196–2	0.1	16.0	38.9
196–3	0.7	16.4	21.1
196–4	0.1	7.8	25.2
196–5	0.3	17.2	40.2
196–7	0.3	17.5	26.4
196–8	0.1	11.2	35.7

Fig. A.2. Compact Tension (CT) specimen

Table A.2
CT specimen dimensions

Parameter	Dimension [mm]
t	8
W	40
C	50
an	12 and 18
A1 = A2	11
B1=B2	24
Ø	10

Test and measurement equipment

The experiments are performed on a 25 kN uniaxial test machine with grips as seen in Figure A.3.
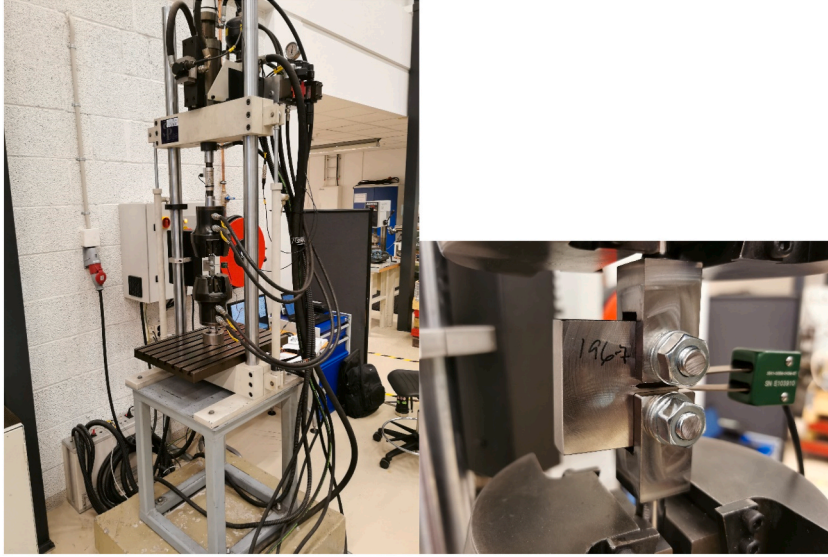
Fig. A.3. Test machine (left), specimen mounted in grips (right)

Compliance measurements

Compliance measurements are performed with a clip gauge mounted at the knife edge on the front face of the specimen. The relationship between deflection at front face of the specimen V_0, the $E - module$, the thickness of the specimen and applied load is given by the following polynomial provided by Saxena and Hudak [50]:

$$\frac{BEV_0}{P} = \left(1 + \frac{0.25}{a/W}\right)\left(\frac{1 + a/W}{1 - a/W}\right)^2 \left\{1.61369 + 12.6778(a/W) - 14.2311\left(\frac{a}{W}\right)^2 - 16.6102\left(\frac{a}{W}\right)^3 + 35.0499\left(\frac{a}{W}\right)^4 - 14.4943(a/W)^5\right\}$$

(A.1)

The polynomial is valid for $0.2 \leq \frac{a}{W} \leq 0.975$.

Measurements were recorded continuously but recommended crack growth intervals given in ISO12108 were utilized when determining the crack growth rate by the secant method.

Appendix B. Basis for establishing regression lines and parameters in the Huang-Moan model

The basis for both linear regressions to establish C and m parameters and for establishing the parameters in the Huang-Moan model is to minimize the square sum of residuals. When test results are plotted against a baseline curve the residual E_i is defined as the vertical distance from the datapoint to the curve ref Fig. 2. The square sum of the residuals is thus defined as:

$$Q^2 = \sum_{i=1}^{n} (E_i)^2$$

(B.1)

The variance of the residuals is defined as:

$$s^2 = \frac{Q^2}{n - 2}$$

(B.2)

where n is the number of datapoints. Finally, the standard deviation, which may be used for establishing confidence intervals for the curves are:

$$s = \sqrt{s^2}$$

(B.3)

In the present work, crack growth experiments are performed at $R = 0.1$, $R = 0.3$ and $R = 0.7$. The following procedure is followed when attempting to collect the test results around a single curve by utilizing ΔK_E:

1. Linear regression of the test results at $R = 0.1$ on a log-log scale
2. Finding the value of β which minimizes the square sum of the residuals (E_i) when expressing the test data for all R-ratios as ΔK_E vs da/dN relative to the $R = 0.1$ curve found from linear regression.
3. Use the obtained value of β to construct a curve for $R = 0$.

To obtain a growth curve corresponding to $R = 0$, the regression line for $R = 0.1$ can be transformed by utilizing the obtained β value. The coefficient C_0 corresponding to $R = 0$ can then be obtained by using a chosen value of ΔK together with the relationships given in equations B.4 and B.5. The slope parameter m is kept as found from the regression analysis. In addition, analyses with m fixed to the value provided by BS7910 is performed.

$$\frac{da}{dN} = C_{0.1}\Delta K^m = C_0 \Delta K_E^m \tag{B.4}$$

$$C_0 = \frac{C_{0.1}\Delta K^m}{\Delta K_E^m} \tag{B.5}$$

Appendix C. Sensitivity study of increment size

The increment size utilized in crack growth simulations in the present work can be written as shown in Eq.C.1 where $X = 20$ is used for the calculations.

$$Cycle\ increment = \frac{X}{(\Delta T/MBL)^2} \tag{C.1}$$

The purpose of this sensitivity study is to see how much influence the increment size has on the simulated number of cycles of crack growth and to evaluate weather the increment size is accurate enough for the present study. The sensitivity study has been performed by utilizing the crack growth model presented in the present work to simulate crack growth from an initial crack of depth 2.9 mm to a final crack size of D/2 at the crown location on a D145mm link. X has been given the values 20, 10, 5 and 2,5 to see the difference in number of cycles between X = 20, which is used for all simulations in the present work, and the other values of X. The results are presented in Figure C.1. As shown in the graphs, the difference in estimated number of cycles between X = 20 and X = 2.5 for mean loads less than or equal to 16% MBL is less than 2.5% and decreasing with decreasing mean load and tension range. For Mean load of 20% MBL the difference is less than 5% for tension ranges of 10% MBL and below, whereas the difference is between 5 and 7% for tension ranges above 15%MBL. Hence, for mean loads of 20% MBL and below, the increment size with X = 20 is accurate enough for most practical purposes. For mean loads of 24% and above the difference in number of cycles is between 5 and 22% and increasing with increasing mean load and tension range. For a simulation where the purpose is to evaluate the safety of a structure containing a crack this is obviously too much difference. Hence, for such cases at high mean loads and high tension ranges, the increment size should be decreased compared to what has been utilized here. On the other hand, for the mean loads above 24%, the crack growth phase is shown to be a small part of the total life of the structure and as such this increment size where X = 20 is utilized is accurate enough for the purpose of the present study.
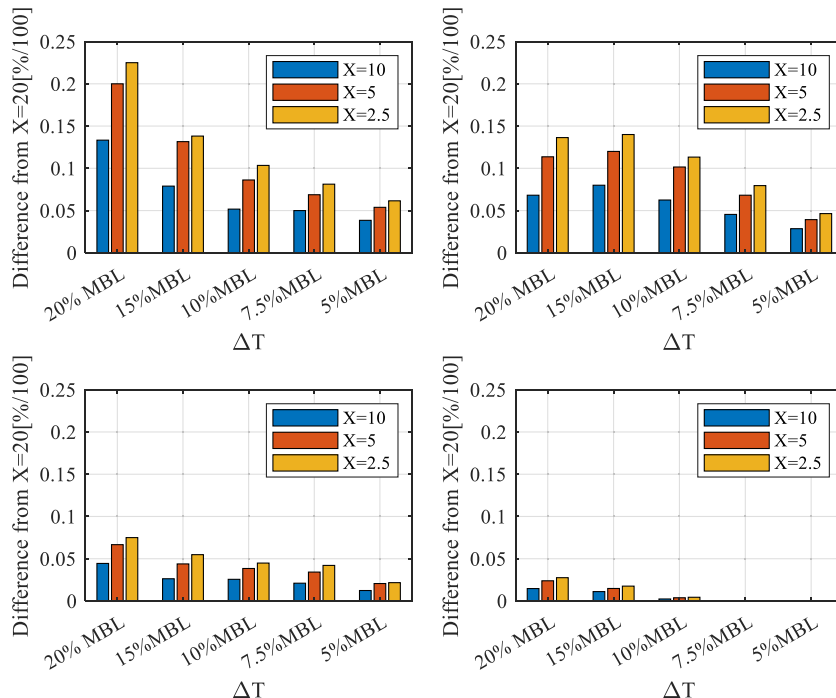
Fig. C.1. Results from sensitivity analysis of increment size for crack growth simulations

Appendix D. Geometry factors for round bars Ref [47]

Axial loading:

$$
\begin{aligned}
Y_{I,Ma}\left(\frac{a}{c},\frac{a}{d}\right) = {} & 1.205 - 0.716\left(\frac{a}{c}\right) - 1.339\left(\frac{a}{d}\right) + 0.19\left(\frac{a}{c}\right)^2 + 0.73\left(\frac{a}{c}\right)\left(\frac{a}{d}\right) + 17.16\left(\frac{a}{d}\right)^2 - 0.1324\left(\frac{a}{c}\right)^2\left(\frac{a}{d}\right) - 0.2841\left(\frac{a}{c}\right)\left(\frac{a}{d}\right)^2 - 40.18\left(\frac{a}{d}\right)^3 \\
& - 2.136\left(\frac{a}{c}\right)^2\left(\frac{a}{d}\right)^2 - 6.817\left(\frac{a}{c}\right)\left(\frac{a}{d}\right)^3 + 51.78\left(\frac{a}{d}\right)^4
\end{aligned}
$$

(D.1)

$$
\begin{aligned}
Y_{I,Mc}\left(\frac{a}{c},\frac{a}{d}\right) = {} & 0.211 + 1.336\left(\frac{a}{c}\right) + 2.204\left(\frac{a}{d}\right) - 0.728\left(\frac{a}{c}\right)^2 - 9.546\left(\frac{a}{c}\right)\left(\frac{a}{d}\right) + 11.84\left(\frac{a}{d}\right)^2 + 4.521\left(\frac{a}{c}\right)^2\left(\frac{a}{d}\right) + 25.18\left(\frac{a}{c}\right)\left(\frac{a}{d}\right)^2 - 51.34\left(\frac{a}{d}\right)^3 \\
& - 12.1\left(\frac{a}{c}\right)^2\left(\frac{a}{d}\right)^2 - 12.45\left(\frac{a}{c}\right)\left(\frac{a}{d}\right)^3 + 66.75\left(\frac{a}{d}\right)^4
\end{aligned}
$$

(D.2)

Bending loading:

$$
\begin{aligned}
Y_{I,Ba}\left(\frac{a}{c},\frac{a}{d}\right) = {} & 1.263 - 0.8196\left(\frac{a}{c}\right) - 4.088\left(\frac{a}{d}\right) + 0.2402\left(\frac{a}{c}\right)^2 + 3.383\left(\frac{a}{c}\right)\left(\frac{a}{d}\right) + 19.04\left(\frac{a}{d}\right)^2 - 1.057\left(\frac{a}{c}\right)^2\left(\frac{a}{d}\right) - 8.698\left(\frac{a}{c}\right)\left(\frac{a}{d}\right)^2 - 37.14\left(\frac{a}{d}\right)^3 \\
& + 0.06085\left(\frac{a}{c}\right)^2\left(\frac{a}{d}\right)^2 + 6.07\left(\frac{a}{c}\right)\left(\frac{a}{d}\right)^3 + 32.13\left(\frac{a}{d}\right)^4
\end{aligned}
$$

(D.3)

$$
\begin{aligned}
Y_{I,Bc}\left(\frac{a}{c},\frac{a}{d}\right) = {} & 0.2293 + 1.315\left(\frac{a}{c}\right) + 0.5773\left(\frac{a}{d}\right) - 0.7197\left(\frac{a}{c}\right)^2 - 6.075\left(\frac{a}{c}\right)\left(\frac{a}{d}\right) + 8.39\left(\frac{a}{d}\right)^2 + 2.187\left(\frac{a}{c}\right)^2\left(\frac{a}{d}\right) + 16.97\left(\frac{a}{c}\right)\left(\frac{a}{d}\right)^2 \\
& - 36.53\left(\frac{a}{d}\right)^3 - 4.423\left(\frac{a}{c}\right)^2\left(\frac{a}{d}\right)^2 - 12.52\left(\frac{a}{c}\right)\left(\frac{a}{d}\right)^3 + 43.38\left(\frac{a}{d}\right)^4
\end{aligned}
$$

(D.4)

Appendix E. FE analysis for determining stresses at fatigue hot spots

Obtaining a good estimate of the residual stresses and the stress range distribution at the crack location and separating the stress distributions into bending and membrane stresses are necessary to obtain a good estimate for K_{res} and ΔK. Chain links manufactured according to the most common class authorities such as ABS and DNV have standard dimensions relative to the diameter D of the chain link. Standard link dimensions have therefore been used to perform stress analysis. The link is modelled with a circular cross section with dimensions shown in Figure E.1. These dimensions are the mean values after proof loading. An actual link will deviate from this due to yielding during proof loading and will have local areas, especially at the contact points between the links where the cross section will not be circular. In addition, the fabrication tolerances will allow for some deviation from this geometry. However, due to the large number of links in a mooring line, using the mean value is a good starting point.
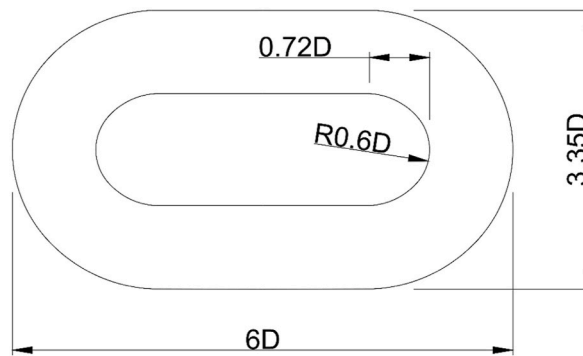

Fig. E.1. Standard dimensions for stud-less common-link

Two analyses must be performed, a non-linear analysis where the proof loading of the link is simulated for obtaining an estimate of the residual stresses and a linear analysis simulating tension loading during service of the link where the corresponding stress distribution is found.

The FEA software ANSYS Workbench was utilized for the analyses. Overview of the parameters for the link utilized in the analyses is seen in Table E.1.

Table E.1
Chain link for analysis

D [mm]	Material	MBL [kN]	Proof Load [kN]	ΔT - Tension range for analysis [kN]	Nominal stress range based on applied tension range [Mpa]
145	R4 (Material 1 and 2)	18,665	13,079	1866.5	57

For the non-linear analysis elastic-plastic material models with multilinear isotropic hardening, ref Figure E.2, were utilized where the parameters for the material model was based on material certificates provided for the chain links utilized for the small-scale experiments and the full-scale experiments in the present work. The E-modulus was set to 207000 MPa.
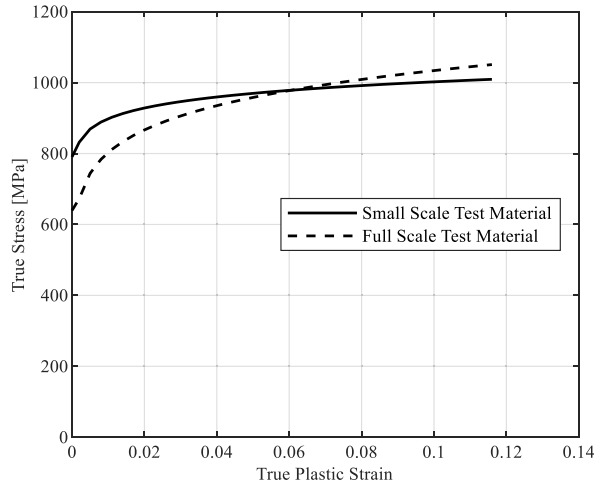

Figure E.2Material model for non-linear analysis

Two links were included in each analysis where only 1/8 of the links was modelled due to symmetry conditions. The load was applied to one link as a remote force, friction contact was applied between the links and all symmetry conditions were modelled as displacements set to 0 in the respective directions. The stresses were retrieved from the link where only symmetry conditions were applied. 10% of the MBL of the chain link was applied as load in the linear analysis. In the non-linear analysis the proof load was reached in the second last time step before the load were reduced to 1000 N in the last time step to ensure contact between the link was obtained but allowing for residual stresses to be determined.
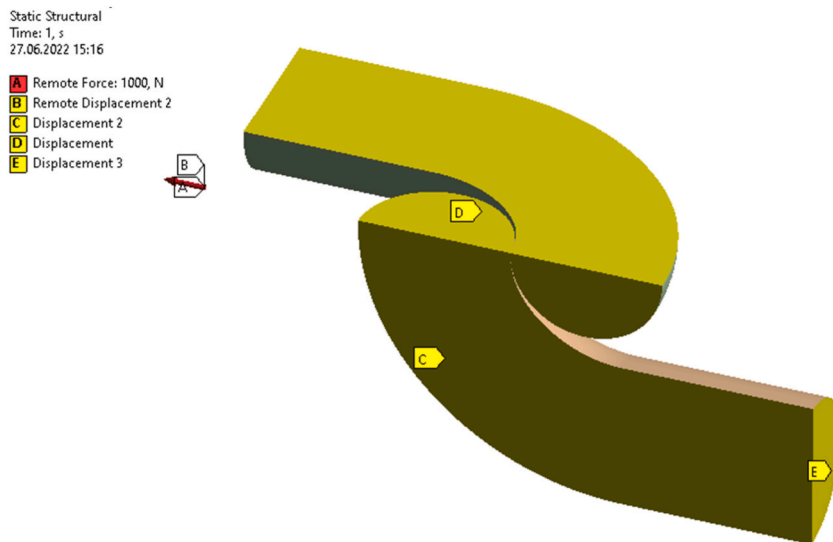

Fig. E.3. Principle figure of FEA model of chain links

From the analyses results, the normal stresses at the crown were separated into bending and membrane stresses respectively. This also involved a linearization process for the residual stresses found from the non-linear analyses. From the linear analysis, stress concentrations factors relative to the nominal stress in the link could be determined and expressions for bending stress and membrane
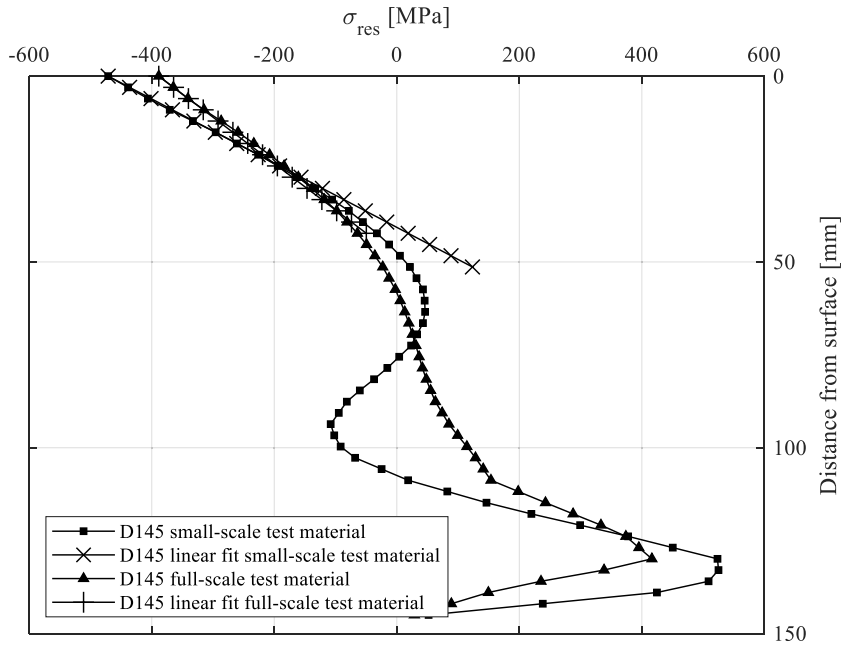
stress at the crown could be obtained.

The nominal stress range in the link which will be referenced to is given by:

$$\Delta\sigma_N = \frac{2\Delta T}{\pi D^2} \tag{E.1}$$

Residual stresses at crown

Following the FE analysis, the normal stress distribution over the cross section at the crown takes the shape shown below, which have been linearized for separating into bending and membrane stress components.

Fig. E.4. Residual stresses at the crown location and linearization

The following values are then obtained for representing the residual stress as membrane and bending stress for calculation K_{res} and subsequently the R-ratio.

Table E.2
Residual stresses separated into bending and membrane stress

	$\sigma_{B,res}$ [mPa]	$\sigma_{M,res}$ [mPa]
Material 1	−839	368
Material 2	−581	192

Stress ranges at crown

Following the linear FE analysis, the normal stress distribution over the cross section at the crown takes the shape shown in .
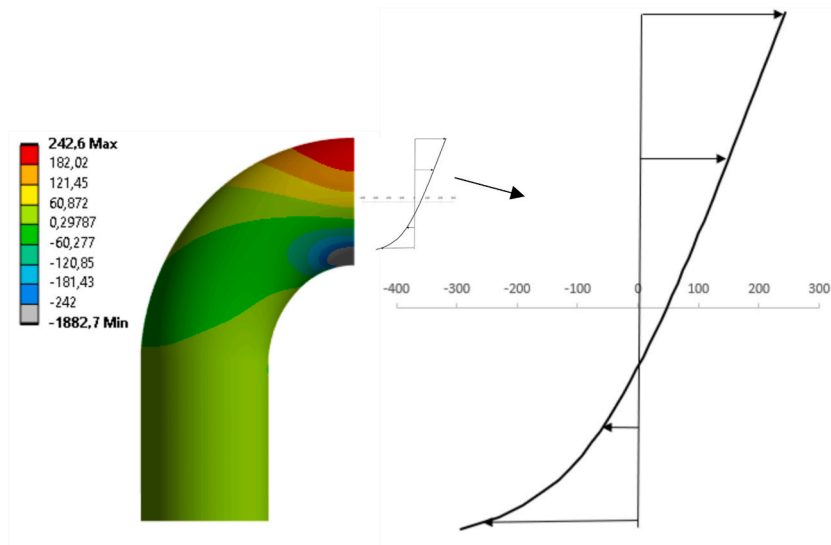
Fig. E.5. Normal stress distribution over the cross section at the crown location

From the centre of the cross section and towards the contact point of the two links the stress distribution has a non-linear shape where large compressive stresses can be seen towards the contact area. The largest compressive stresses are omitted from the graph due to the high magnitude. However, the stress distribution is almost linear from the centre of the cross section and towards the crown. Hence, the bending stress and the membrane stress contributions are established based on the upper part of the distribution. Separate stress concentration factors (SCF) can then be retrieved for bending and membrane stress by relating the different contributions to the nominal stress of the link and thus to the diameter of the link.

Table E.3

Obtained stress ranges and SCFs at the crown from FE analyses

D [mm]	$\Delta\sigma_{tot}$ [Mpa]	$\Delta\sigma_B$ [Mpa]	$\Delta\sigma_M$ [Mpa]	$SCFB$	$SCFM$	SCF total
145	242.6	195.5	47.14	3.458	0.834	4.29

The total stress concentration factor compare very well with the work of Zhang and Smedley found in Ref. [7].

When combining the nominal stress range with the stress concentration factors found for bending and membrane stress ranges respectively, the separated stress ranges at the crown can be written as:

$$\Delta\sigma_{B,crown} = \frac{6.916\Delta T}{\pi D^2} \tag{E.2}$$

And

$$\Delta\sigma_{M,crown} = \frac{1.668\Delta T}{\pi D^2} \tag{E.3}$$

References

[1] Ma K, Luo Y, Kwan T, Wu Y. Mooring system engineering for offshore structures. 2019.
[2] Zarandi EP, Skallerud BH. Experimental and numerical study of mooring chain residual stresses and implications for fatigue life. Int J Fatig 2020;135:105530.
[3] Perez IM, Bastid P, Venugopal V. Prediction of residual stresses in mooring chains and its impact on fatigue life. Omae-2017; 2017. p. 1–10.
[4] Qvale P, Zarandi EP, Arredondo A, Ås SK, Skallerud BH. Effect of cyclic softening and mean stress relaxation on fatigue crack initiation in a hemispherical notch. Fatig Fract Eng Mater Struct Dec. 2022;45(12):3592–608.
[5] Gabrielsen Ø, Larsen K, Reinholdtsen S-A. Fatigue testing of used mooring chain, vol. 1. Offshore Technol.; 2017, V001T01A072.
[6] Ma K, et al. Fatigue tests on corroded mooring chains retrieved from various fields in offshore west africa and the North Sea. Proc. ASME 2019 38th Int. Conf. Ocean. Offshore Arct. Eng. 2019:1–17.
[7] Zhang YH, Smedley P. Fatigue performance of high strength and large diameter mooring chain in seawater. In: Proceedings of the international conference on offshore mechanics and arctic engineering - omae, vol. 3; 2019. p. 1–11.
[8] Gabrielsen Ø, Larsen K, Dalane O, Lie HB, Reinholdtsen S-A. Mean load impact on mooring chain fatigue capacity: lessons learned from full scale fatigue testing of used chains. Proc. ASME 2019 38th Int. Conf. Ocean. Offshore Arct. Eng. 2017:1–8. 2019.
[9] Lone EN, Leira BJ, Sauder T, Aksnes V, Gabrielsen Ø, Larsen K. Influence of mean tension on mooring line fatigue life. In: ASME 2020 39th international conference on ocean, offshore and arctic engineering; 2020. 03-Aug.

[10] Gabrielsen Ø, Reinholdtsen S-A, Skallerud B, Haagensen PJ, Andersen M, Kane P-A. Fatigue capacity of used mooring chain – results from full scale fatigue testing at different mean loads. In: Proceedings of the ASME 2022 41st international conference on ocean. Hamburg, Germany: Offshore and Arctic Engineering OMAE2022 June 5-10; 2022. 2022.

[11] Lone EN, Sauder T, Larsen K, Leira BJ. Fatigue assessment of mooring chain considering the effects of mean load and corrosion. In: ASME 2021 40th international conference on ocean, offshore and arctic engineering; 2021. 21-Jun.

[12] Lone EN, Sauder T, Larsen K, Leira BJ. Probabilistic fatigue model for design and life extension of mooring chains, including mean load and corrosion effects. Ocean Eng Feb. 2022;245:110396.

[13] Fernández J, Storesund W, Navas J. Fatigue performance of grade R4 and R5 mooring chains in seawater. Proc. Int. Conf. Offshore Mech. Arct. Eng. - OMAE2014 2014;23491(45370):V01AT01A035.

[14] Hørte T, Okkenhaug S. Recommendations for a fatigue design analysis calibrated using structural reliability analysis. In: Proceedings of the ASME 2022 41st international conference on ocean. Hamburg, Germany: Offshore and Arctic Engineering OMAE2022 June 5-10; 2022. 2022.

[15] Miller KJ. The three thresholds for fatigue crack propagation. In: Piascik RS, Newman JC, Dowling NE, editors. Fatigue and fracture mechanics: 27th volume. West Conshohocken, PA: ASTM International; 1997. p. 267–86.

[16] Miller KJ, Akid R. The application of microstructural fracture mechanics to various metal surface states. Proc. R. Soc. London. Ser. A Math. Phys. Eng. Sci. 1949; 452:1411–32. Jun. 1996.

[17] Suresh S, Ritchie RO. Propagation of short fatigue cracks. Int Met Rev Jan. 1984;29(1):445–75.

[18] DNV. Offshore standard DNV-OS-E301 - Position Mooring. July 2021.

[19] Almar-Næss A. Fatigue handbook: offshore steel structures. 1.st. 1985. Tapir.

[20] Smith RA, Miller KJ. Fatigue cracks at notches. Int J Mech Sci 1977;19(1):11–22.

[21] Qvale P, Zarandi EP, Ås SK, Skallerud BH. Digital image correlation for continuous mapping of fatigue crack initiation sites on corroded surface from offshore mooring chain. Int J Fatig 2021;151:142–1123.

[22] Hobbacher AF. Recommendations for fatigue design of welded joints and components, 2.nd. Springer Cham; 2016.

[23] British Standards Institution. BS 7910:2013+A1:2015, Guide to methods for assessing the acceptability of flaws in metallic structures. 2015.

[24] Dowling NE. Notched member fatigue life predictions combining crack initiation and propagation. Fatig Fract Eng Mater Struct Sep. 1979;2(2):129–38.

[25] Mikulski Z, Hellum V, Lassen T. Modeling the fatigue damage evolution in welded joints. 2017, V004T03A009. 57687.

[26] Mikulski Z, Lassen T. Fatigue crack initiation and subsequent crack growth in fillet welded steel joints. Int J Fatig 2019;120:303–18.

[27] Lassen T, Canada L, Arana JL, Henriksen J. Crack growth in high strength chain steel subjected to fatigue loading in. Omae; 2005. p. 1–9.

[28] Zhang Y-H, Zettlemoyer N, Tubby PJ. Fatigue crack growth rates of mooring chain steels. In: Proceedings of the ASME 2012 31st international conference on ocean. Offshore and Arctic Engineering; 2012.

[29] Paris P, Erdogan F. A critical analysis of crack propagation laws. J. Basic Eng. Dec. 1963;85(4):528–33.

[30] Chowdhury P, Sehitoglu H. Mechanisms of fatigue crack growth – a critical digest of theoretical developments. Fatig Fract Eng Mater Struct Jun. 2016;39(6): 652–74.

[31] Elber W. The significance of fatigue crack closure. In: Rosenfeld MS, editor. Damage tolerance in aircraft structures. West Conshohocken, PA: ASTM International; 1971. p. 230–42.

[32] Richie RO. Mechanisms of fatigue crack propagation in metals ceramics and composites: role of crack tip shiedling. Mater. Sci. Eng. A 1988;103(1):15–28.

[33] C. H. N. RW Hertzberg R Jaccard, Crack closure: correlation and confusion. West Conshohocken, PA: ASTM International.

[34] Vasudevan AK, Sadananda K. Analysis of fatigue crack growth under compression–compression loading. Int J Fatig 2001;23:365–74.

[35] Silva FS. The importance of compressive stresses on fatigue crack propagation rate. Int J Fatig Oct. 2005;27(10–12):1441–52.

[36] Walker K. The effect of stress ratio during crack propagation and fatigue for 2024-T3 and 7075-T6 aluminum. In: Rosenfeld MS, editor. Effects of environment and complex load history on fatigue life. West Conshohocken, PA: ASTM International; 1970. p. 1–14.

[37] Kujawski D. A fatigue crack driving force parameter with load ratio effects. Int J Fatig 2001;23:239–46.

[38] Kujawski D. A new $(\Delta K + K_{max})0.5$ driving force parameter for crack growth in aluminum alloys. Int J Fatig 2001;23(8):733–40.

[39] Huang X, Moan T. Improved modeling of the effect of R-ratio on crack growth rate. Int J Fatig 2007;29(4):591–602.

[40] Huang X, Moan T, Cui W. A unique crack growth rate curve method for fatigue life prediction of steel structures. Ships Offshore Struct 2009;4(2):165–73.

[41] Adedipe O, Brennan F, Kolios A. A relative crack opening time correlation for corrosion fatigue crack growth in offshore structures. Fatig Fract Eng Mater Struct Apr. 2016;39(4):395–411.

[42] ISO. ISO 12108, Third edition 2018-07, Metallic materials - fatigue testing- Fatigue crack growth method. 2018.

[43] Vosikovsky O. Effects of mechanical and environmental variables on fatigue crack growth rates in steel. A summary of work done at canmet. Can Metall Q Jan. 1980;19(1):87–97.

[44] Zhang Y-H, Doré M. Fatigue crack growth assessment using BS 7910:2013 - background and recommended developments. Int J Pres Ves Pip 2018;168:79–86.

[45] Carpinteri A. Shape change of surface cracks in round bars under cyclic axial loading. Int J Fatig 1993;15(1):21–6.

[46] Couroneau N, Royer J. Simplified model for the fatigue growth analysis of surface cracks in round bars under mode I. Int J Fatig 1998;20(10):711–8.

[47] Hellum V, Lassen T, Spagnoli A. Crack growth models for multiaxial fatigue in a ship's propeller shaft. Eng Fail Anal Sep. 2021;127:105470.

[48] DNV Offshore standard. DNV-OS-E302 - Offshore mooring chain. July. 2022.

[49] Fernández J, Arredondo A, Storesund W, González JJ. Influence of the mean load on the fatigue performance of mooring chains. In: Offshore technology conference; 2019, D011S014R002. 06-May.

[50] Saxena A, Hudak SJ. Review and extension of compliance information for common crack growth specimens. Int J Fract 1978;14(5):453–68.